Online ISSN: 2981-0396 Print ISSN: 2981-0388

International Journal of Iron & Steel Society of Iran

Journal Homepage: https://journal.issiran.com/

Research Article

The Effect of Carbon Content on the Solidification of Steel Slabs in the Continuous Casting Process: A Numerical Simulation Case Study

A. Pourfathi *[1]

Department of Materials Science and Engineering, Sharif University of Technology, Tehran, Iran

ARTICLE INFO

Keywords:

Numerical Simulation, Heat Transfer, Continuous Casting, Steel Slab, Metallurgical Length, Thickness Factor, Carbon Content, CALPHAD.

Article history:

Received 05 July 2024
Received in revised form 10 July 2025
Accepted 04 August 2025

ABSTRACT

In this study, the effect of carbon content, the primary element in the chemical composition of carbon steel grades, on the solidification of steel slabs is investigated using a numerical simulation approach. Three commercial carbon steel grades with varying carbon contents are selected. Technological and operational conditions, such as slab geometry, water flow rates of spray nozzles in the secondary cooling zone, mold features, casting speed, and the temperature of spray cooling water in the secondary cooling zone, are held constant and based on a real industrial continuous slab casting machine. The thermophysical properties of each steel grade are computed based on the calculation of phase diagrams (CALPHAD). The numerical simulation of the process is then conducted by solving the heat transfer equation (coupled with the CALPHAD-based thermophysical properties) based on computational fluid dynamics (CFD) simulated in the MATLAB environment. Parameters such as metallurgical length and solid shell thickness profiles are calculated and compared over time for various steel grades. In addition, the factor K in the famous square root function for solid shell thickness (as a function of time) is determined and analyzed for each grade. This study demonstrates that increasing the carbon content decreases the metallurgical length. As carbon content decreases, the thickness factor K increases in carbon steel grades.

1. Introduction

One of the most important processes in materials science and engineering is the casting method, which is interestingly associated with heat transfer and phase change phenomena in metals and alloys. Since the dawn of the industrial era, casting has been used to produce metallic and alloy products, such as ingots, slabs, billets, and blooms, which serve as initial materials in forming techniques. Two methods are employed to manufacture these materials: 1) ingot casting and 2) continuous casting. Although ingot casting has been used to make ingot products, the invention of the continuous casting machine (CCM) in the 1800s revolutionized slab casting methods. Since World War two, the ingot casting method has been replaced with the continuous casting (CC) method extensively due to 1) high production speed, 2) less human force, 3) being cost-effective, and 4) high quality of the products, for example, finer grain size, higher mechanical properties, less segregation, and to

* *Corresponding Author*
Email: pourfathi.ali@gmail.com
Address: Department of Materials Science and Engineering, Sharif University of Technology, Tehran, Iran
1. Ph. D.

DOI: http://10.22034/IJISSI.2025.2034632.1296
Published by ISSI (Iron & Steel Society of Iran)

name but a few. It should be noted that about 96% [1] of steel products produced by CCM are consumed in transportation, aerospace, petrochemical, automotive, mining, construction (for example, bridge-building) industries, and to name but a few.

In the continuous steel casting process, after steelmaking, the molten steel is transported to the tundish, and later, it is cast from the tundish into the water-cooled copper mold via a submerged entry nozzle. The mold, called the primary cooling zone, has no bottom; in fact, the surface of the mold cools the molten steel at its interface. Hence, although a solid shell forms around the molten steel, the core remains liquid, referred to as the strand in casting literature. After mold, the strand proceeds to the secondary cooling zone (SCZ), where water cooling sprays sprinkle water droplets to cool and solidify the whole strand. Then, the strand is cut at the torch cut-off point and transmitted to stock (Fig. 1-a). The top level of the melt in the mold is referred to as the meniscus. The path the strand takes from the meniscus to where the last melt droplet (on the central axis of the strand) is solidified is called the metallurgical length or liquid pool (see the yellow area inside the strand in Fig. 1).

The quality of casting slabs depends on different variables: the geometry of the slab, chemical composition, casting speed, water flow rates in nozzles of the secondary cooling zone, the water temperature, the water velocity in the water-cooled copper mold, the temperature of inlet water and outlet water of the mold, and to name but a few. As the secondary cooling zone is longer than the mold, it is more important and effective in controlling and reducing the casting defects in the strand. Researchers in the literature have investigated the influences of working and metallurgical factors and how to regularize them to produce a sound product. As empirical efforts are time-consuming and costly, simulation methods are economical and almost precise in predicting, controlling, and optimizing the process. One of the most critical cases in the process is the decrease in casting speed due to the displacement of ladles, which causes temperature fluctuations and the formation of casting defects. Due to such challenges, foundrymen and researchers have attempted to regulate water flow rates in SCZ to minimize fluctuations in the water flow rates. One approach is to employ simulation and control methods, such as feedback or closed-loop control techniques, to mitigate thermal variation [3, 4]. The open-loop control method is used to investigate a control strategy for reducing thermal fluctuations, and the simulation demonstrates the validity of the model [5, 6]. In addition, the customary proportional integral derivative (PID) method has been employed to establish suitable water flow rates for SCZ sprays, thereby controlling the surface temperature and simulating the temperature field [7-12]. Another

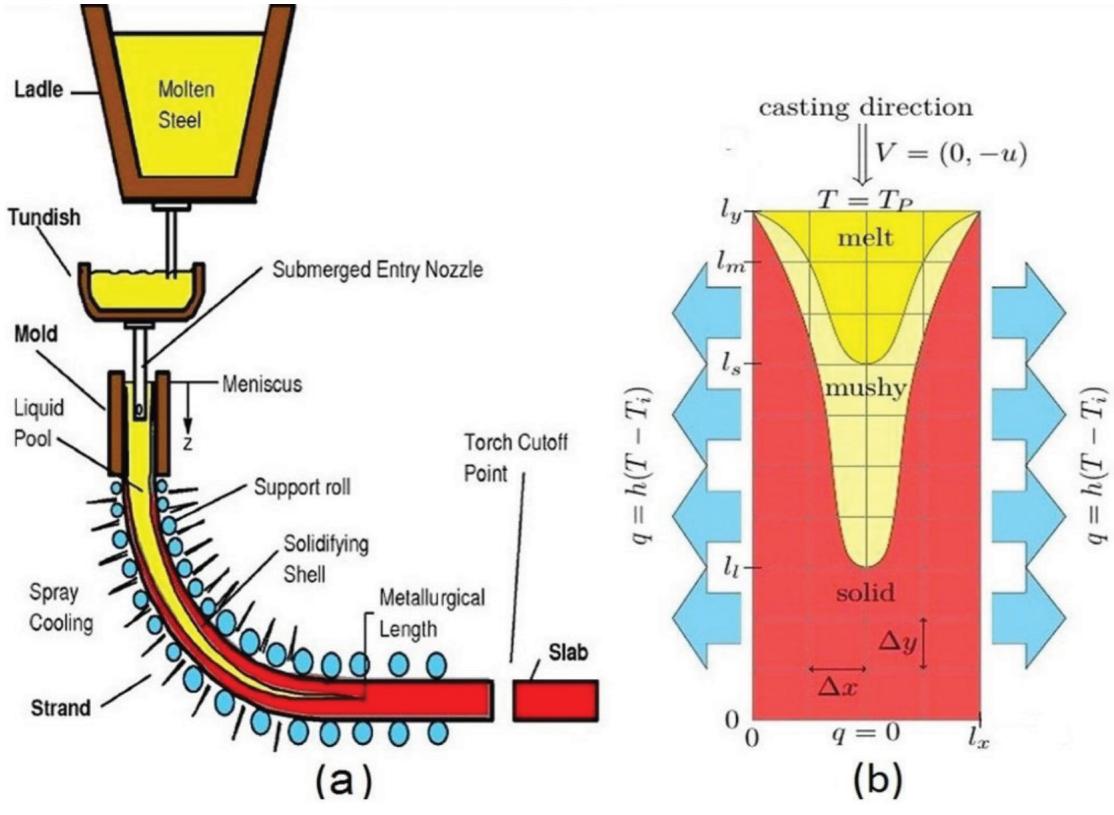

Fig. 1. a) Vertical continuous casting of steel [2] and b) A schematic illustration of vertical slab casting (thickness-length cross-section).

famous procedure is the Alternating-direction implicit (ADI) controlling algorithm, as shown in [13], which is a helpful method to harmonize the CCM's working factors and to simulate the surface temperature under a calculated fixed casting speed. Several simulations of the CCM are based on data from numerical optimization techniques, which are the core of inverse problems. In this study, inverse heat transfer problems (IHTP) are considered. The genetic algorithm is employed in the literature to reduce cracks in slabs, and the results are validated through using numerical simulations [14,15].

Additionally, it has been previously demonstrated that using a numerical projected gradient-based algorithm can be a suitable method for minimizing porosities [16]. In [17], the effect of casting speed change on the mechanical behavior of the strand is simulated using finite element methods on the condition that the metallurgical length is fixed under casting speed change (based on energy conservation law). The literature indicates that both numerical and analytical solutions of the two-phase one-dimensional Stephan problem for the CC process of steel are identical [5, 18-20]. In this regard, the solid shell formed during cooling in both zones using numerical simulation conforms acceptably with the analytical equation as follows:

$$x = K\sqrt{t} \qquad \text{Eq.(1)}$$

Where t(min), x(mm), and K(m $min^{-0.5}$) denote time, solid shell thickness, and thickness factor important for foundrymen to estimate metallurgical length to predict the location of cracks and segregation. As previously mentioned, the quality of casting slabs depends on different variables. For example, regarding the effect of the slab thickness, the author demonstrated that the higher the slab thickness, the longer the metallurgical length, and the higher the coefficient K [21]. Although the influence of other variables is studied in the literature, the effect of the steel grades' carbon content on the slab's solidification and the factor K in Eq.(1) is not investigated clearly. However, to the best of our knowledge, the literature does not contain studies or research on the effect of carbon content (the principal element of steel). Therefore, the effect of carbon content on different steel grades is examined. Indeed, three different commercial steel grades with varying carbon content are selected in the present work. The geometry of slabs, the water flow rate of nozzles, and casting conditions in primary and secondary cooling zones are assumed to be identical for all steel grades. Thermophysical properties for each grade are calculated separately based on computational thermodynamics theory, known as CALPHAD[1] , using the frequently used commercial software package JMatPro. Later, these data are coupled in a computer program, including coding an algorithm to solve the heat transfer PDE using numerical techniques. Accordingly, the metallurgical length and the thickness factor K are computed and compared for the chosen steel grades.

2. Mathematical Model for Heat Transfer

In the first place, in order to simulate the CC process, the physical assumptions considered in this work, similar to the author's previous work [21], are proposed as follows:

1. The thermal model is assumed to be transient (similar to reference [21], with which validation will be conducted later). As noted in [21], validated by [22], the beginning of the slabs' CC process was overlooked due to the application of a steady-state thermal model. Although the condition is transient when the process begins, its duration is negligible compared to the whole time of the CC process in one sequence. However, we consider the transient model here to make the model more comprehensive.
2. The effect of rolls is not considered.
3. The influence of fluid dynamics is ignored. Indeed, the Navier-Stokes equation is not solved in this model; however, its impacts on the heat transfer of the mushy zone[2] and melt pool are imposed on thermal conductivity by an effective factor that will be described later.
4. It is well-known that slab casting simulation can be conducted in three and two dimensions [23], although both methods yield the same results. The two-dimensional model is preferred because of the trivial thermal gradient along the width and length as compared with that along the width and length. Here, similar to [20], the two-dimensional model is considered.
5. As the CCM considered in this study has large radii, the effect of internal and external radii on heat transfer is negligible [15]. Therefore, a specific computational domain with its boundary conditions is considered vertical in this study (see Fig. 1. (b) and Fig. 2).
6. Although the heat transfer mechanisms are complex in the CC process, in several studies in the literature [for example, see 24, 25, 26, 27, 28], three zones are considered as follows: primary (mold) zones, SCZ (or water-cooling zones), and free zone (or air-cooling zone). For SCZ and free zones (or air-cooling zones), convection and radiation are the dominant mechanisms, respectively. Our study assumes that there is neither free zone nor roll contact; both include radiation as the dominant heat transfer mechanism [24, 25, 26, 27, 28]. Instead, we assume that the whole area below the mold is SCZ. Therefore, based on the literature [24, 25, 26, 27, 28] and our previous consideration (that the area below the mold to torch cut-off point is considered SCZ thoroughly), we assume that convection is the dominant heat mechanism beneath the mold and that radiation is

1. CALculation of PHAse Diagrams
2. In alloys with a solidification range, the zone between solid and liquid temperature is called the mushy zone, acting like a porous media.

negligible.

7. Thermophysical properties will be assumed to be temperature-dependent in this study. Accordingly, as the density of steel is temperature-dependent, the inlet melt flow would have a different velocity compared to the outlet solid at casting speed. However, a constant velocity is assumed for the melt and solidifying slab throughout the design domain.

The computational domain, symbolized as Ω, the frame of reference, the origin of the coordinate system (0,0), and boundaries Γ_t, Γ_l, Γ_b, and Γ_s are shown in Fig. 2. According to this figure, Γ_t, Γ_l, Γ_b, and Γ_s denote the upper boundary (pouring area), lateral boundaries (the interphase between cooling zones and the strand), the bottom area of the slab (torch cut-off point), and the symmetrical boundary. For the sake of less computational cost, the calculation is conducted for the half slab, and the symmetry boundary condition is considered (see dotted line in Fig. 2). In fact, $\partial\Omega = \Gamma_t \cup \Gamma_l \cup \Gamma_b \cup \Gamma_s$ such that $\Gamma_t \cap \Gamma_l = \emptyset, \Gamma_t \cap \Gamma_b = \emptyset, \Gamma_t \cap \Gamma_s = \emptyset, \Gamma_l \cap \Gamma_s = \emptyset, \Gamma_b \cap \Gamma_s = \emptyset$ and $\Gamma_b \cap \Gamma_l = \emptyset$. In the present work, a two-dimensional transient heat transfer equation accompanied by boundary conditions is stated hereunder:

Eq.(2)

$$\begin{aligned}
\rho\, c_e(\vec{V}\cdot\nabla T + \frac{\partial T}{\partial t}) &= \nabla\cdot(k\nabla T) && \text{in } \Omega && \text{(a)}\\
-k\nabla T\cdot\vec{n} &= h\,(T - T_i) && \text{on } \Gamma_l && \text{(b)}\\
-k\nabla T\cdot\vec{n} &= 0 && \text{on } \Gamma_b && \text{(c)}\\
-k\nabla T\cdot\vec{n} &= 0 && \text{on } \Gamma_s && \text{(d)}\\
T &= T_P && \text{on } \Gamma_t && \text{(e)}
\end{aligned}$$

Where $k\left(\frac{\mathrm{W}}{\mathrm{m}\cdot\mathrm{K}}\right)$, T(K), T_P(K), $\vec{V}(\frac{\mathrm{m}}{\mathrm{s}}) = (0, v)$, $\rho(\frac{\mathrm{Kg}}{\mathrm{m}^3})$, $h(\frac{\mathrm{W}}{\mathrm{m}^2\cdot\mathrm{K}})$, t(s) and $c_e(\frac{\mathrm{J}}{\mathrm{Kg}\cdot\mathrm{K}})$ denote thermal conductivity, temperature, pouring temperature, casting speed, density, heat transfer coefficient, time, and apparent heat capacity (or equivalent specific heat capacity). Thermophysical properties are affected by some phase transformation phenomena in materials. The literature [16, 21, 29] proposes several typical formulae as follows:

$$H(T) = (1 - f_l(T))\int_{T_r}^{T} \rho c_s\, dT + f_l(T)\int_{T_r}^{T} \rho c_l\, dT + f_l(T)\rho L_f \qquad \text{Eq.(3)}$$

$$c_e = c_p + L_f\frac{df_l(T)}{dT} \qquad \text{Eq.(4)}$$

Where H(T), L_f, and c_p denote the enthalpy, the latent heat of fusion, and specific heat capacity. L_f is not a fixed value or independent of temperature; thus, this typical formula is not generally correct. Furthermore, these typical formulae are limited because they do not consider the latent heat of solid-state phase transformations, e.g., peritectic reaction in peritectic steel grades. Moreover, the explicit form of f_l is unavailable for many commercial casting alloys (see [29]). The general form of H(T) and other thermophysical data are computed based on the CALPHAD approach to resolve these limitations. Hence, the latent heat of fusion and other phenomena are included in the thermal model's thermophysical properties (c_e, ρ, and H(T)) [29]. The model was previously used by the author [21]. Also, the effect of latent heat of fusion is evident in the graphs of Fig. 3., Fig. 4. and Fig. 5. (which will be discussed later. See the abrupt changes of thermophysical properties within the mushy zone in Fig. 3., Fig. 4., Fig. 5. and the temperature difference between solidus and liquidus, to understand the effect of the latent heat of fusion). Regarding Eq.(4), it should be noted that some research studies employ the typical, explicit formulae to calculate the thermophysical parameter c_e in Eq.(2) (for example, see [22]). However, other studies apply c_e by incorporating the temperature relationship obtained from the CALPHAD method (or Differential Scanning Calorimetry (DSC)); this method is well-known as "Apparent Heat Capacity" (AHC). Hence, from now on, we call c_e "AHC" (Eq.(3) is only used to calculate the AHC, and the enthalpy is not used in the heat transfer equation).

As previously mentioned, the effect of melt momentum is ignored, but its influence is embedded in thermal conductivity as follows:

$$k = f_s\, k(T) + m\, f_l\, k(T) \qquad \text{Eq.(5)}$$

Where f_s, f_l, and m are solid volume fraction, liquid volume fraction, and effective factor of fluid momentum on the heat transfer of molten steel. The parameter m is considered between 5 and 7 in the literature, and, according to [30], 7 is considered here.

3. Numerical Modeling

The slab is assumed two-dimensional, and Eq.(2) along with its boundary conditions must be solved on the computational domain in Fig. 2. First, the computational grid must be generated on the domain, and later, the heat transfer equation is discretized using the finite difference method (FDM). Symbols as L_x(m), L_y(m), L_z(m), n_x, n_y, and n_z, denote thickness, width, length, the number of discretizing points along the thickness, the number of discretizing points along the width, and the number of discretizing points along the length. Additionally, $\Delta x = L_x/n_x$, $\Delta y = L_y/n_y$, $\Delta z = L_z/n_z$ denote the dimensions of each computational cell. As the fully explicit FDM method is used here to discretize the heat transfer PDE,

we must keep the stability of the solution and guarantee its convergence because the fully explicit FDM is sensitive to the time step. As there are both convection and diffusion terms in the thermal model, the time step, Δt, in the model is the minimum value of the two criteria as the diffusive time step, Δt_{Diff}, and Courant–Friedrichs–Lewy (CFL) time step, Δt_{CFL} [31, 32]. It can be stated as follows [31,32]:

Eq.(6)

$$\Delta t_{CFL} = \frac{1}{2}\min\left(\frac{\Delta x}{v_x/2}, \frac{\Delta y}{v_y/2}\right) \quad \text{(a)}$$

$$\Delta t_{Diff} = \frac{1}{2}\left[\frac{\min\left(\rho(T)\right)\ \min\left(c_p(T)\right)\ \left(\min(\Delta x, \Delta y)\right)^2}{4\ \max(k)}\right] \quad \text{(b)}$$

$$\Delta t \leq \min(\Delta t_{CFL}, \Delta t_{Diff}) \quad \text{(c)}$$

The time step is sensitive to mesh size and thermophysical properties. The time step is calculated for each steel grade because their thermophysical properties are different (the term includes time in Eq.(2-b), and $\frac{\partial T}{\partial t}$ is discretized using the forward difference method). As the heat transfer equation is transient here, in order for the numerical solution to stably converge to the steady state answer, the convergence criterion is expressed as the absolute error (infinity norm) of the temperature field between two successive time steps as follows:

$$\left\|T^{n+1} - T^{n}\right\|_{\infty} < \varepsilon \quad \text{Eq.(7)}$$

Where ε and n denote the threshold of the convergence criterion and the time counter.

The slab's geometry (produced in a real CCM of the SMS Demag company and used in this study [23]) and numerical parameters are shown in the Table 1. In order for the simulation results to approach reality, thermophysical properties such as density, apparent heat capacity, and liquid volume fraction are extracted directly as a function of temperature. To obtain these data, the commercial JMatPro software package based on theories of computational thermodynamics and the minimization of total Gibbs energy, see Fig. 3., Fig. 4. and Fig. 5. As we are supposed to investigate the effect of carbon content on the heat transfer, the chemical analysis of three different steel grades, including low-, mild-, and high-carbon steels, is considered, see Table 2. The liquidus temperature, the solidus temperature, and their difference (as the length of the mushy zone) are demonstrated in the Table 3. for each steel grade (These

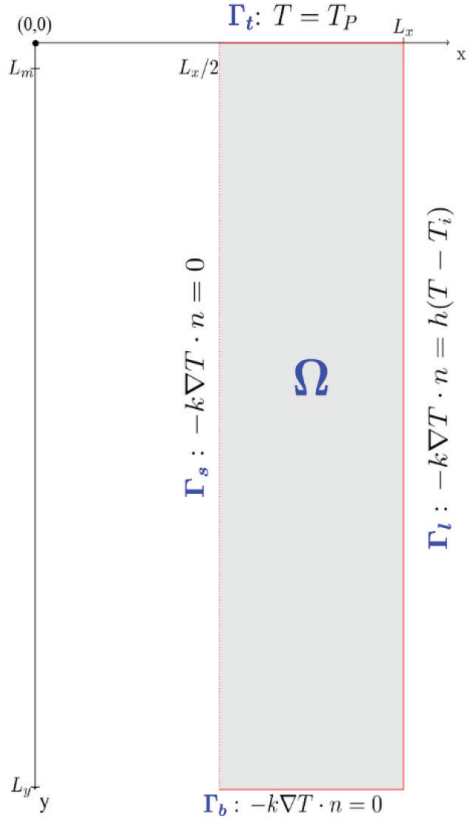

Fig. 2. Computational domain (thickness-length cross-section of the slab) with its boundary conditions, coordinate system, and frame of reference used in the present work (the figure is not a scale model of the real strand, and it is entirely schematic).

data are extracted from the abrupt jump in liquid volume fraction graphs with respect to temperature in Fig. 3., Fig. 4. and Fig. 5.). Also, as the chemical composition, primarily carbon content, is the only variable in this work, all of the other variables, such as the water flow rate of all nozzles in SCZ and technological conditions for all grades, are assumed to be identical. Hence, the values of water flow rates for each segment of SCZ are expressed in the Table 4. SCZ includes 12 cooling segments with cooling nozzles, the patterns of which are the same.

Similarly, the cooling condition of the mold is identical for all steel grades. In the mold, according to a [22], the following equation is widely used to calculate the amount of heat flux transfer between the mold and the strand:

$$Q = 2400000 - 346000\sqrt{L_m/v} \qquad \text{Eq.(8)}$$

Where L_m (m), v $(\frac{\mathrm{m}}{\mathrm{min}})$, and Q $(\frac{\mathrm{W}}{\mathrm{m}^2})$denote the length of the mold, casting speed, and mold heat flux, respectively.

Table 1. The numerical parameters and the geometry used in this work.

L_x(m)	L_y(m)	L_z(m)	L_m(m)	v(m/min)	n_x	n_y	n_z	ω	ε	T_i(°C)
0.2	26.74	0.9	0.9	1.3	40	200	80	0.5	0.001	25

Table 2. Chemical analysis (weight percent or wt%) of the selected steel grades in this study.

Steel grade	C	Si	Mn	P	S	Ni	Mo	N	Cr	Nb	Cu	Al
AISI/SAE 1010	0.12	0.03	0.5	0.015	0.015	0.04	0.1	0.006	0.04	0.005	0.04	0.06
St 50	0.28	0.2	0.6	0.035	0.35	-	-	-	-	-	-	-
Ck 75	0.8	0.2	0.7	0.025	0.025	0.4	0.1	0.009	0.4	-	-	-

Table 3. Solidus, liquidus temperatures, and the temperature difference of selected steel grades in this study.

Steel grade	T_s(°C)	T_L(°C)	Temperature difference(°C)
AISI/SAE 1010	1474	1524	50
St 50	1351	1466	115
Ck 75	1433	1506	73

Table 4. Lengths and water flow rates of each segment in the secondary cooling zone (data obtained from the catalog of the SMS Demag machine).

Sprays	Length (m)	Water flow rate (L/min)
Foot roller	0.2	380.5
segment 1	1.35	553
segment 2	2.13	277.2
segment 3	1.99	718.5
segment 4	2.01	480
segment 5	2.01	480
segment 6	2.19	339.5
segment 7	2.2	339.5
segment 8	2.2	242.7
segment 9	2.2	242.7
segment 10	2.48	295.2
segment 11	2.48	295.2
segment 12	2.48	295.2

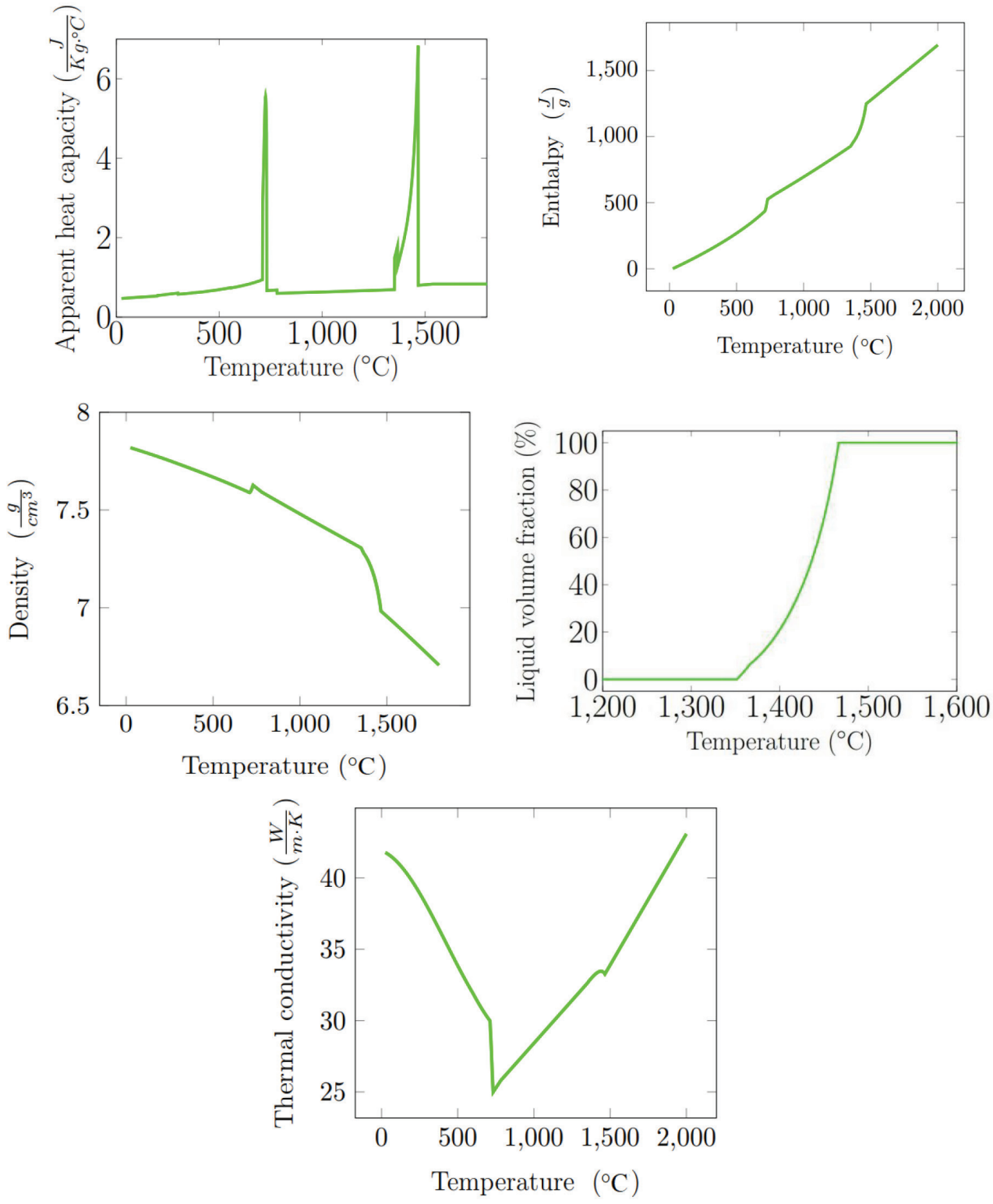

Fig. 3. Thermophysical properties of AISI/SAE 1010 steel grade based on the CALPHAD technique.

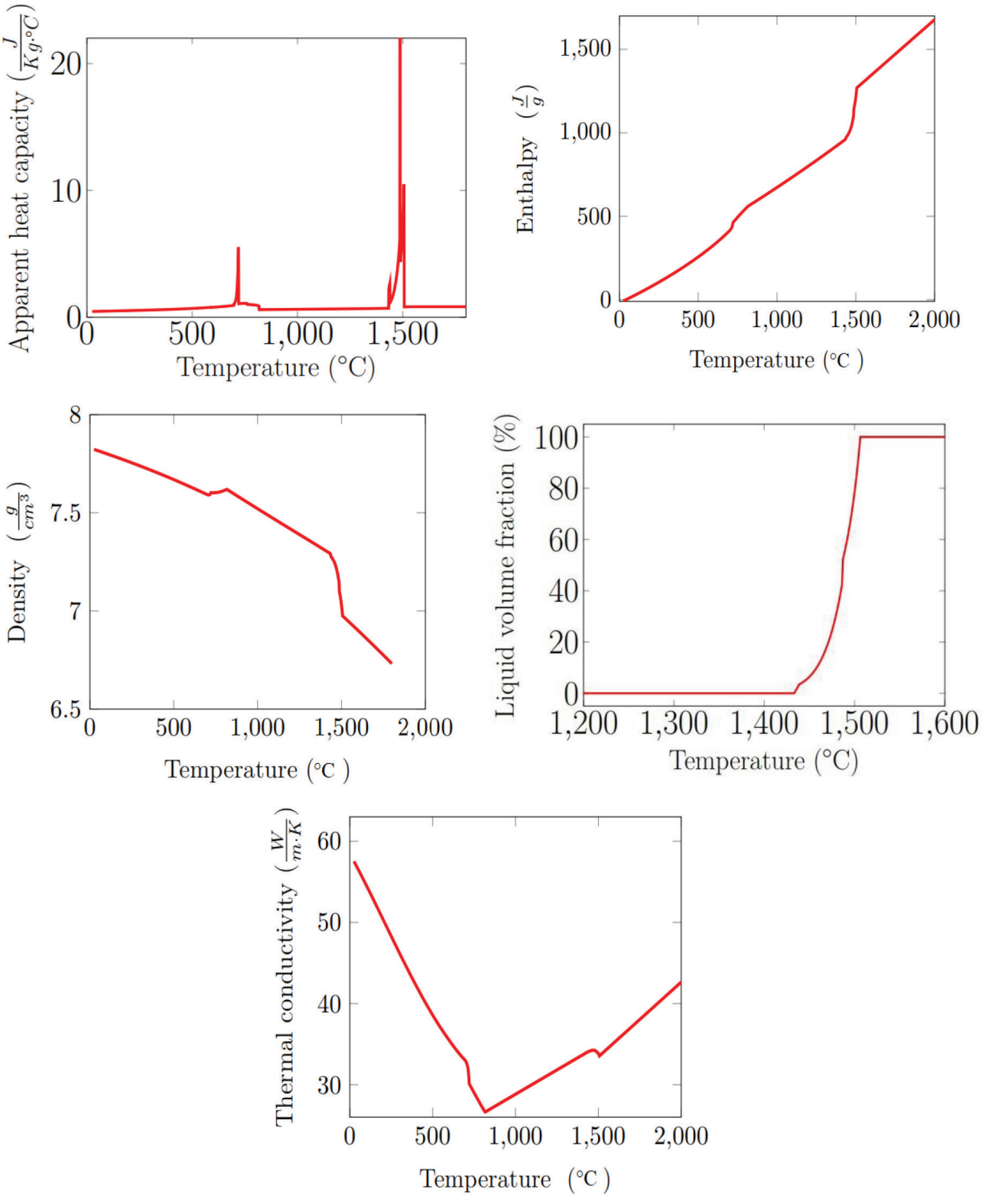

Fig. 4. Thermophysical properties of St50 steel grade based on the CALPHAD technique.

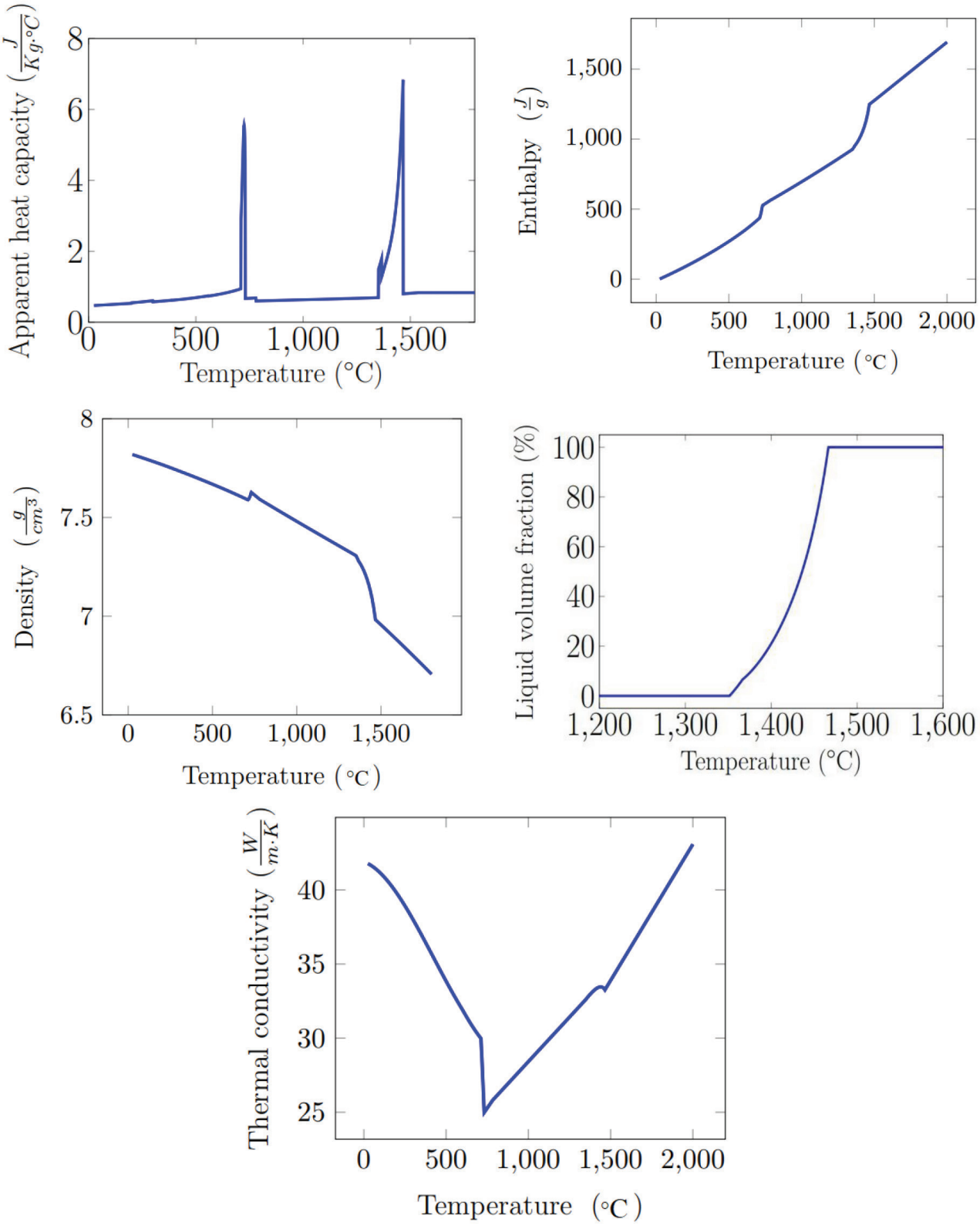

Fig. 5. Thermophysical properties of Ck75 steel grade based on the CALPHAD technique.

In Eq.(2-b), the convective heat transfer coefficient, h, must be imposed on the equation to simulate the process. In order to find the parameter for each segment, a well-known equation called the Nozaki relation is used in the literature as follows [33]:

$$h = \frac{1570\ \dot{w}^{0.55}\ (1\ -0.0075\ T_i)}{\alpha} \qquad \text{Eq.(9)}$$

Where α is the machine calibration factor considered a value around 4 to 6, and α equals 4 in this study for slab casting [16, 21]. Also, $h(\frac{W}{m^2 \cdot K})$, $\dot{w}(\frac{L}{m^2\ s})$, and T_i (K) denote heat transfer coefficient, water spray density, and the temperature of cooling nozzle water in SCZ. It should be noted that water spray density differs from water flow rate such that water spray density is obtained by dividing water flow rate by the area of the spray on the slab surface. More precisely, the factor α is determined by measuring empirical data and applying IHTP methods to each segment. However, it is widely agreed in the literature that α=4 is approximately appropriate for steel slab casting [34, 35]. The variation of heat transfer coefficient concerning distance from the meniscus is plotted in Fig. 6. using Eq.(9), Table 4. and considering T_i=25°C. Additionally, casting speed is considered to be 1.3 m/min, conforming to industrial data (extracted from the CCM catalog). As the internal and external curves of the CCM are so large, their possible effects on the heat transfer are negligible (more details are available in [23]). Therefore, the computational domain has been considered vertical (as mentioned previously in the assumptions). The discretization method is based on fully explicit FDM, and the computer program is scripted in MATLAB.

Mesh sensitivity analysis is one of the most crucial analyses to ensure the accuracy of the numerical results based on the FDM employed in this work. Mesh dependency is crucial, as it can significantly impact the final results of the simulation. Mesh density must not be too fine, as a mesh that is too fine can increase computational cost and time, and decrease computational efficiency. Additionally, mesh density should not be too coarse, as a coarse mesh can introduce significant errors and instability into the numerical solution. Therefore, an optimal mesh density must be obtained using grid dependency analysis. Indeed, as we solve partial differential equations using approximations all the time, our solution might have some errors. Minimizing errors requires conducting a mesh dependency analysis to determine the optimal number of computational costs. In this regard, mesh sensitivity analysis is described in Appendix A, showing that selecting n_x=80 and n_y=200 is an optimal choice for mesh density. The mesh density refers to the total number of computational cells as $n_x \times n_y$ in this study. The reader is referred to Appendix A for more details.

3.1. Model Validation

As previously mentioned, the model used in this study is similar to those used in [21, 22]. To ensure the current model is practical, validation is conducted as described in [21]. Data such as chemical composition, machine geometry, and slab thickness (23 cm), among others, are extracted from reference [22]. The thermophysical data is the only difference between the current model and the model proposed in [22]. This difference also applies to the model in [21]. In fact, [22] used typical formulas for thermophysical properties (for example, Eqs.(3), (4) and others (in the literature) that do not consider the effect of material phenomena discussed in the section on a mathematical model for heat transfer in this work). However, the CALPHAD method is used in both [21] and the current model to calculate near-reality thermophysical properties. The calculation formulas for mold heat flux and heat transfer coefficient, water flow rate, and cooling water temperature of the nozzles in the current work and [21] are identical to those in [22]. After doing the simulation using the current thermal model for a low-carbon steel grade used in both [21] and [22], the result is shown in Fig. 7. and Fig. 8. According to these graphs, the metallurgical length calculated using the current model is about 20.1m close to that of [22] as 19.9m. Additionally, the calculated values of shell thickness based on the current model and [22] are compared with the measured thickness in [22] at three different points, as shown in the Table 5. The uncertainty is computed as a mean relative error of around 9.34%, which is acceptable. The formula for the calculation of uncertainty is as follows:

$$\text{Mean relative error} = \frac{1}{N}\sum_{i=1}^{N}\frac{\left|x_{\text{experimental}} - x_{\text{simulated}}\right|}{x_{\text{experimental}}} \qquad \text{Eq.(10)}$$

In addition, according to Fig. 7. there is a difference between the calculated surface and centerline temperature values in the current model and those of [22]. Considering the uncertainties, as indicated by the mean relative error (stated above) between the simulated data using the current model and the data in [22], the uncertainties for the graphs in Fig. 7. are estimated to be approximately 7% and 6% for the surface and core temperature profiles, respectively.

The differences and uncertainties mentioned in the above calculations can be rooted in the thermophysical properties. As previously mentioned, we have employed the CALPHAD technique, which is more realistic, to calculate thermophysical data, despite the typical formula used for these properties in [22]. Although it may not be possible to estimate uncertainty, especially in numerical methods such as FDM, the uncertainties reported above are relatively small and acceptable.

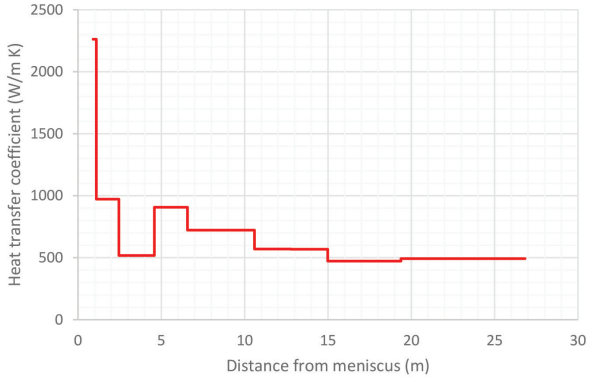

Fig. 6. Variation of heat transfer coefficient with respect to distance from the meniscus.

Table 5. A comparison of shell thickness obtained using the current model and reference [22] at three points.

Distance from meniscus (m)	Shell thickness (m)		
	Reference [22]		The current model
	Simulation	Experiment	Simulation
5.679	0.060149	0.065	0.048859
17.2	0.097656	0.095	0.096374
19.6	0.111042	0.112	0.113964

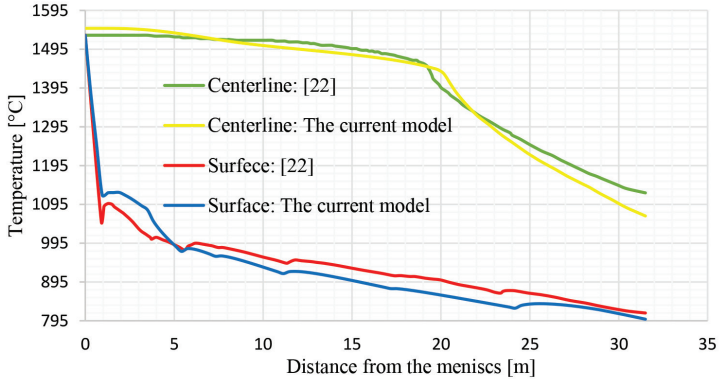

Fig. 7. Comparison of simulated centerline temperature profiles (yellow and green) and simulated surface temperature profiles (red and blue) between the present work and [22].

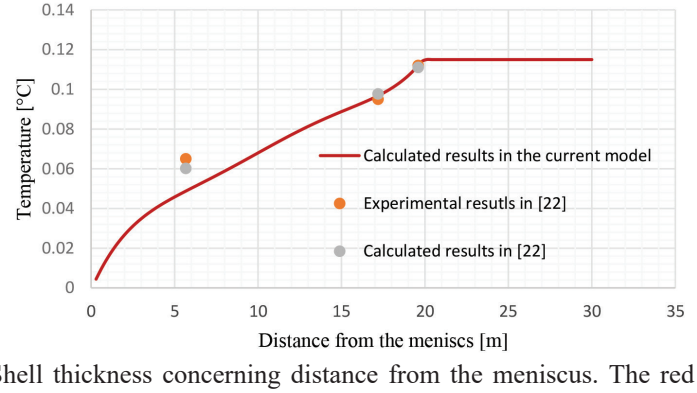

Fig. 8. Comparison of Shell thickness concerning distance from the meniscus. The red curve corresponds to the simulation in this study; both the experimental data (orange points) and simulated data (gray points) are extracted from [22].

4. Results and discussion

4.1. Solidification and Metallurgical Length

Schematic contours of temperature and liquid volume fraction for the length-thickness cross section are shown in Figs. 9 and 10 (these figures are scaled along the x and y directions with 0.1905 and 0.0047 coefficients, respectively). The simulated metallurgical lengths for AISI/SAE 1010, St50, and Ck75 are approximately 19.07m, 16.91m, and 14.77m, respectively. It is evident that in identical working conditions, AISI/SAE 1010 has the longest metallurgical length, and Ck75 has the shortest metallurgical length. Also, the metallurgical length of St50 is more than that of Ck75 and less than that of AISI/SAE 1010. Therefore, by increasing the carbon content in steel grades, the metallurgical length is reduced. By increasing the carbon content of low carbon steel, either mild carbon or high carbon steel, the metallurgical length declines, which might cause defect formation of the slab's surface during the unbending of the strand. It proved that different and suitable water flow rates must be employed for each steel grade. In fact, for each steel grade with a specific carbon content (or chemical analysis) and evident working conditions, the water flow rate of nozzles in SCZ for the steel grade differs from that for another chemically different steel grade in identical technological circumstances. Indeed, producing sound steel grades with different carbon content and identical water flow rates cannot be expected.

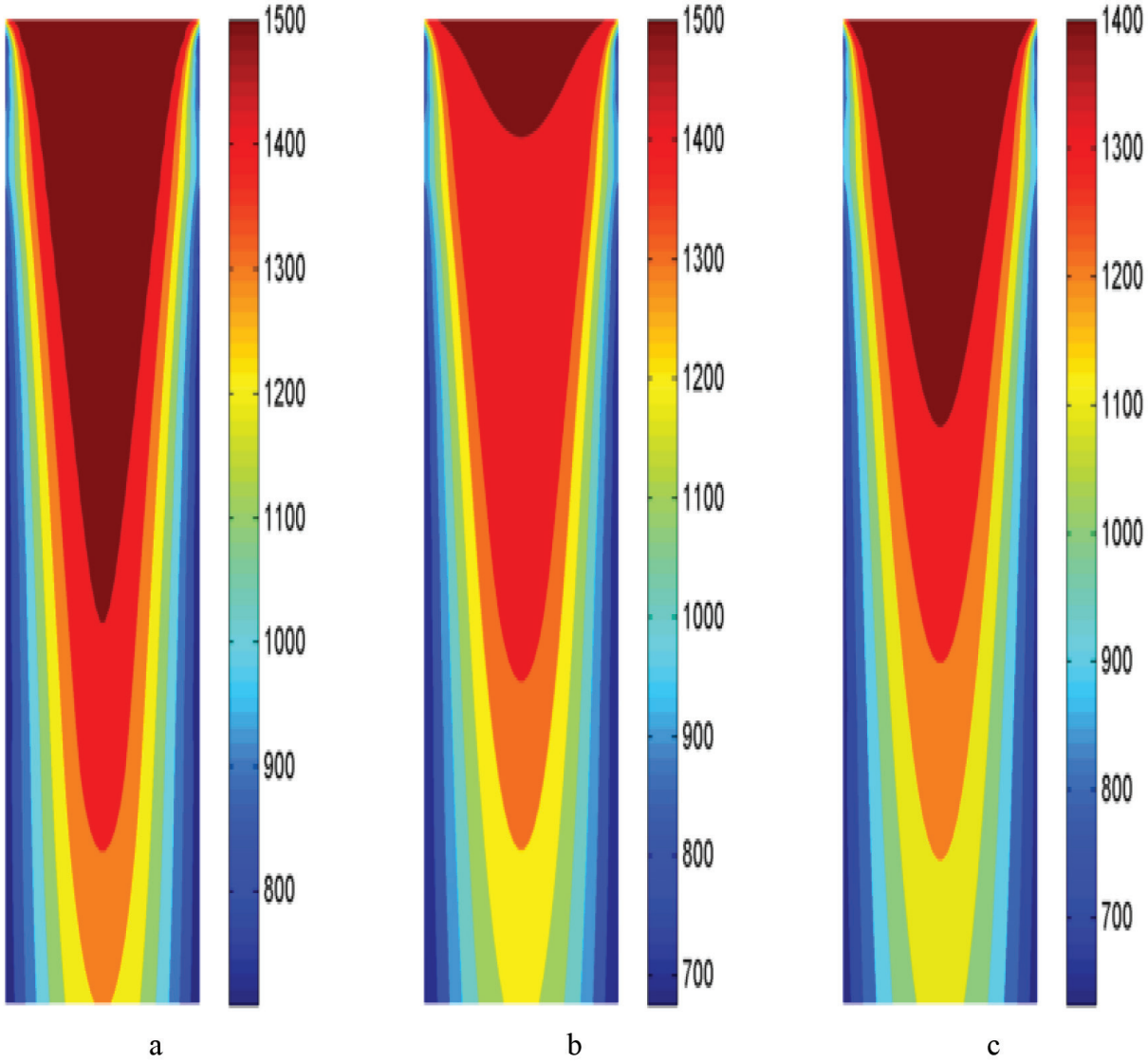

Fig. 9. Temperature contours of length-thickness cross section in the mid-width position of the slab: a) AISI/SAE 1010, b) St50, and c) Ck75. The scale coefficients along the x and y directions are 0.1905 and 0.0047, respectively.

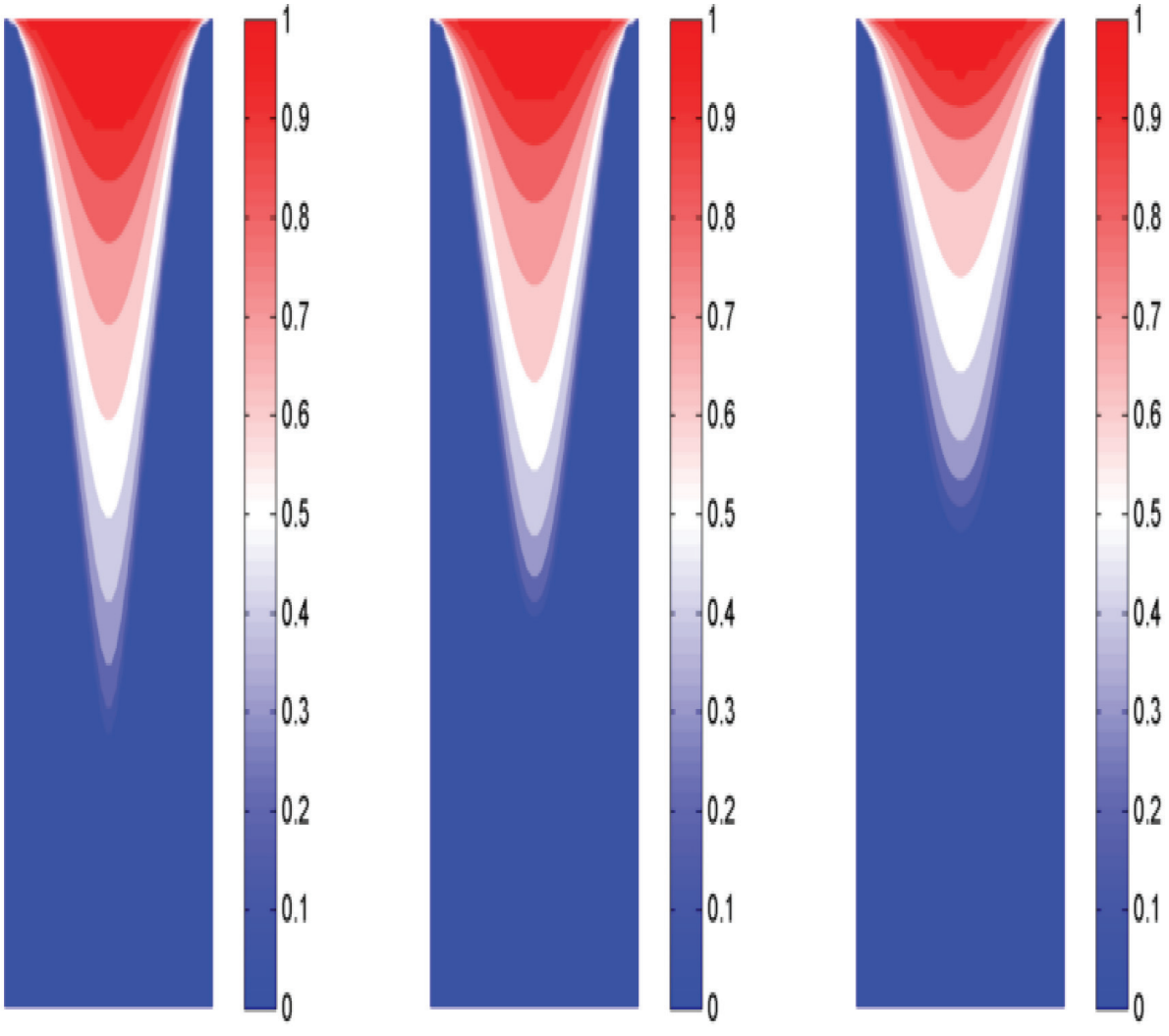

Fig. 10. Liquid volume fraction contours of length-thickness cross section in the mid-width position of the slab: a) AISI/SAE 1010, b) St50, and c) Ck75. The scale coefficients along the x and y directions are 0.1905 and 0.0047, respectively.

4.2. Solid shell thickness and thickness factor, K

The black graphs of Fig. 11. show the solid shell thickness as a function of time as the strand proceeds downward. As already stated, Eq.(1) has been confirmed in the literature, and the foundrymen use it to predict the metallurgical length and the location of potential cracks and segregations. Accordingly, the values of K for each steel grade are estimated using a straightforward fitting technique of Eq.(1) on the data gained by the simulation for AISI/SAE 1010, St50, and Ck75 as 25.3, 27.7, and 29.7, respectively. According to these results, adding more carbon to the steel grades increases the coefficient K. Regarding the method of fitting, the reader is referred to Appendix B. Based on the fitting method described in Appendix B and Eq.(B-3) in Appendix B, the standard error of fitting for AISI/SAE 1010, St50, and Ck75 is calculated as 2.39%, 2.44%, and 2.5%, respectively. As uncertainty, the mean relative fitting error for AISI/SAE 1010, St50, and Ck75 is computed as 13.79%, 19.35%, and 17.15%, respectively. The uncertainties can be rooted in not considering radiation (as in roll contact and the air-cooling zone) in our model (see the assumptions previously expressed in the section on the mathematical model for heat transfer).

Regarding factor K, in practice, as high-carbon and mild-carbon steels are more sensitive to defect formation, an attempt is made to lengthen the metallurgical length of high-carbon and mild-carbon steels longer than that of low-carbon steel. Although this study aims to investigate the effect of carbon content on identical water flow rates and working conditions, the values of K in the industry differ. The water flow rates for each steel grade in CC plants are regulated differently. The K factor rises by increasing the carbon element from low carbon to mild carbon and from mild carbon to high carbon grade.

Table 6. shows that as the metallurgical length increases, the coefficient K increases. By symbolizing ML and K as the metallurgical length and coefficient K, Table 6. shows the following relation between the effect of carbon content (chemical analysis) and the two metallurgical parameters (ML and K) considered in this study.

$$(ML_{\text{high carbon steel}}) < (ML_{\text{mild carbon steel}}) < (ML_{\text{low carbon steel}})$$
$$(K_{\text{high carbon steel}}) > (K_{\text{mild carbon steel}}) > (K_{\text{low carbon steel}})$$

The higher a steel grade's carbon content, the shorter its metallurgical length and the higher its coefficient K.

Table 6. The calculated coefficient K, metallurgical length, and carbon content for each steel grade studied in the current study are shown.

Steel grade	Carbon content (wt%)	Coefficient K (m. min$^{-0.5}$)	Metallurgical length (m)
AISI/SAE 1010	0.12	25.3	19.072
St 50	0.28	27.7	16.91
Ck 75	0.8	29.7	14.77

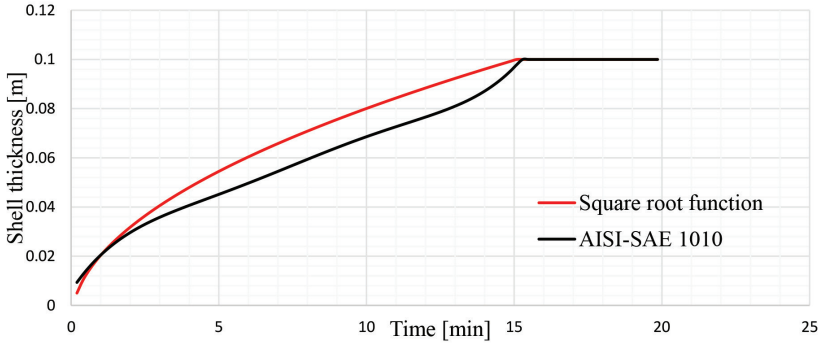

(a)

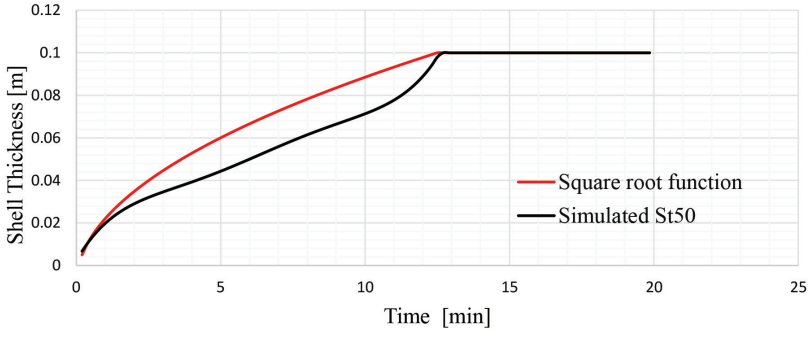

(b)

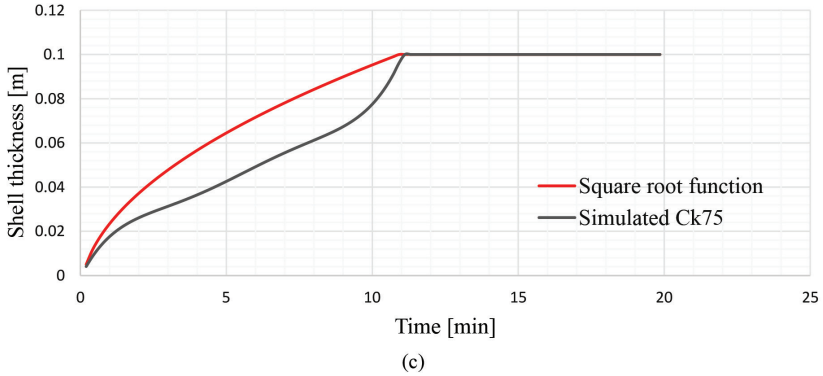

(c)

Fig. 11. Black: solid shell thickness as a function of time as the strand proceeds; red: fitted (or estimated) metallurgical length according to $x = K\sqrt{t}$. a) AISI/SAE 1010, b) St50, and c) Ck75.

5. Conclusions

Carbon content in the chemical composition of steel grades is one of the most important variables influencing the quality of products in the steel CC process. In this study, the impact of carbon content is investigated while fixing all conditions of the CCM. Three different steel grades, including low, mild, and high carbon, are selected for numerical study of their solidification behavior using computer simulation. All working conditions, including water flow rates in SCZ, slab geometry, mold features, and others, are considered identical for all steel grades. The thermophysical properties required to solve the heat transfer PDE are based on computational thermodynamics and the CALPHAD technique and are extracted from the JMatPro software package. The results have shown that the more carbon is added to steel grades, the shorter the metallurgical length and the higher the thickness factor, K. According to the results, the same water flow rate can be used for different steel grades. Instead, the slab casting conditions of low-, mild-, and high-carbon steel grades, such as cooling strategies and water flow rates in SCZ, must be correctly regularized. Additionally, the methodology used in this work to determine the coefficient K in $x = K\sqrt{t}$ for every carbon steel can help the CC manufacturers monitor and, more precisely, inspect the highly probable defect-prone locations in their quality control tests. According to the results of this study, by increasing the amount of carbon element in a steel grade, the metallurgical length increases, and the coefficient K decreases. In other words, the more carbon content a steel grade contains, the less metallurgical length it has, and the higher the coefficient K. It should be noted there is a limitation of the numerical method proposed in this work; i.e., the fully explicit FDM is susceptible to AHC (because CFL criteria does not see the sudden changes of AHC). As the AHC method is used to simulate heat transfer, the AHC method is suspicious, not for the material properties issues, but for the sudden jumps in the diagram AHC vs T. Indeed, grid spacing or a time-step is sensitive to these jumps because the AHC curve is suspicious to bypass the peaks between two nodes, or time steps. Thus, a very high resolution of grid spacing or very small time steps are needed for a reliable simulation, which demands the use of computers with high RAM memory usage. However, this method may not be computationally cost-effective. Instead, other applicable, appropriate mathematical techniques could be used to alleviate this suspicion (or the peaks), which will be the topic of our future research studies.

Nomenclature

$\vec{V}$ Casting velocity vector

v The absolute value of casting speed

T Temperature field

T_P Pouring temperature

T_i The cooling water temperature

ρ Density

k Thermal conductivity

c_p Specific heat capacity

c_e Apparent heat capacity

k Thermal conductivity

h The heat transfer coefficient

Q Heat flux

n_x Mesh size along the thickness

n_y Mesh size along the length

n_z Mesh size along the width

l_x The thickness of the slab

l_y The length of the slab

l_m The thickness of the mold

l_z The width of the slab

$\dot{w}$ Water flow rate

α The calibration factor of the continuous casting machine

t Time

x_s Shell thickness

K The coefficient in the square root function of time and shell thickness

L_f The latent heat of fusion

f_l Liquid volume fraction

$\vec{n}$ The outward unit normal vector on a surface

Ω The computational domain corresponding to the slab

Δx The size of the computational cell along the thickness direction

Δy The size of the computational cell along the length direction

Γ_t The top boundary of the computational domain

Γ_l The lateral boundary of the computational domain

Γ_b The bottom boundary of the computational domain

Γ_s The symmetrical boundary of the computational domain

D Distance from the meniscus

ML The metallurgical length

References

[1] Zappulla M.L, Cho S.M, Koric S, Lee H.J, Kim S.H, Thomas B.G, Multiphysics modeling of continuous casting of stainless steel, Journal of Materials Processing Technology. 2020; 278: 116469.

[2] Huang X, Thomas B.G, Modeling of steel grade transition in continuous slab casting processes, Metallurgical Transactions B. 1993; 24: 379-93.

[3] Santos C.A, Spim J.A, Garcia A, Mathematical modeling and optimization strategies (genetic algorithm and knowledge base) applied to the continuous casting of steel, Engineering applications of artificial intelligence. 2003; 16(5-6): 511-27.

[4] Long M.J, Chen D.F, Zhang J, Ouyang Q, Novel online temperature control system with closed feedback loop for steel continuous casting. Ironmaking & Steelmaking. 2011; 38(8): 620-9.

[5] Long M.J, Chen D.F, Zhang J, Ouyang Q, Novel online temperature control system with closed feedback loop for steel continuous casting, Ironmaking & Steelmaking. 2011; 38(8): 620-9.

[6] Klimeš L, Štětina J, A rapid GPU-based heat transfer and solidification model for dynamic computer simulations of continuous steel casting, Journal of Materials Processing Technology. 2015 ; 226: 1-4.

[7] Louhenkilpi S, Mäkinen M, Vapalahti S, Räisänen T, Laine J, 3D steady state and transient simulation tools for heat transfer and solidification in continuous casting, Materials Science and Engineering: A. 2005; 413: 135-8.

[8] Zheng K, Petrus B, Thomas B.G, Bentsman J, Design and implementation of a real-time spray cooling control system for continuous casting of thin steel slabs. In: AISTech 2007, Steelmaking Conference Proceedings; 2007 May 7; Indianapolis, IN. Warrendale (PA): Association for Iron and Steel Technology.

[9] Yang J, Xie Z, Ji Z, Meng H, Real-time heat transfer model based on variable non-uniform grid for dynamic control of continuous casting billets, ISIJ international. 2014; 54(2): 328-35.

[10] Petrus B, Zheng K, Zhou X, Thomas B.G, Bentsman J, Real-time, model-based spray-cooling control system for steel continuous casting, Metallurgical and materials transactions B. 2011; 42: 87-103.

[11] Männikkö T, Laitinen E, Neittaanmäki P, Real-time simulation and control system for the continuous casting process. In: System Modelling and Optimization: Proceedings of the 14th IFIP Conference; 1989 Jul 3–7; Leipzig, GDR. Berlin: Springer-Verlag; 1990. p. 809–17.

[12] Laitinen E, Neittaanmäki P, Männikkö T, On the real-time simulation and control of the continuous casting process. In: Proceedings of the Third European Conference on Mathematics in Industry; 1990. Dordrecht: Springer Netherlands; 1990. p. 401–8.

[13] Guo L.L, Tian Y, Yao M, Shen H.F, Temperature distribution and dynamic control of secondary cooling in slab continuous casting. International Journal of Minerals, Metallurgy and Materials. 2009 ;16(6): 626-31.

[14] Jauhola M, Kivela E, Konttinen J, Laitinen E, Louhenkilpi S, Dynamic secondary cooling model for a continuous casting machine. InMETEC Congress 94. 2 nd European Continuous Casting Conference. 6 th International Rolling Conference. 1994; 1: 196-200.

[15] Zhai Y.Y, Li Y, Ma B.Y, Yan C, Jiang Z.Y, The optimisation of the secondary cooling water distribution with improved genetic algorithm in continuous casting of steels, Materials Research Innovations. 2015;19: S1-26.

[16] Worapradya K, Thanakijkasem P, Optimum spray cooling in continuous slab casting process under productivity improvement. In: 2009 IEEE International Conference on Industrial Engineering and Engineering Management; 2009 Dec 8; Hong Kong. Piscataway (NJ): IEEE; 2009. p. 120–4.

[17] Pourfathi A, Tavakoli R, Thermal optimization of secondary cooling systems in the continuous steel casting process, International Journal of Thermal Sciences. 2023; 183: 107860.

[18] Bellet M, Salazar-Betancourt L, Jaouen O, Costes F, Modelling of water spray cooling. Impact on thermomechanics of solid shell and automatic monitoring to keep metallurgical length constant. In8th ECCC, European Continuous Casting Conference. 2014:1202-1210.

[19] Spitzer K.H, Harste K, Weber B, Monheim P, Schwerdtfeger K, Mathematical model for thermal tracking and on-line control in continuous casting, ISIJ international. 1992; 32(7): 848-56.

[20] Lalitha S, Chattopadhyay S, Das S.K, Godiwalla K.M, Simulation of heat-transfer in the continuous-casting mold, Transactions of the Indian Institute of Metals. 1991; 44(1): 89-92.

[21] Hejazi J, Ingot Casting (in persian). Iranian Foundrymen Society. 1983.

[22] Pourfathi A, The Effect of Slab Thickness on the Solidification of Low carbon Steel in Continuous Casting Process: A Simulation Case Study, International Journal of Iron & Steel Society of Iran. 2022 ; 19(1): 67-80.

[23] Yu Y, Luo X, Zhang H.Y, Zhang Q, Dynamic optimization method of secondary cooling water quantity in continuous casting based on three-dimensional transient nonlinear convective heat transfer equation, Applied Thermal Engineering. 2019; 160: 113988.

[24] Brimacombe J.K, Continuous casting. THE IRON STEEL SOC. AIME. 1984.

[25] Ramírez-López A, Aguilar-López R, Palomar-Pardavé M, Romero-Romo M.A, Muñoz-Negrón D, Simulation of heat transfer in steel billets during continuous casting. International Journal of Minerals, Metallurgy, and Materials. 2010; 17: 403-16.
[26] Mazumdar D, Ghosh A, Mathematical modelling of heat transfer phenomena in continuous casting of steel, ISIJ international. 1993; 33(7): 764-74.
[27] Kumar M, Roy S, Panda S.S, Numerical simulation of continuous casting of steel alloy for different cooling ambiences and casting speeds using immersed boundary method, Proceedings of the Institution of Mechanical Engineers, Part B: Journal of Engineering Manufacture. 2017; 231(8): 1363-78.
[28] Oksman P, Yu S, Kytönen H, Louhenkilpi S, The effective thermal conductivity method in continuous casting of steel, Acta Polytechnica Hungarica. 2014; 11(9): 6-22.
[29] Louhenkilpi S, Laitinen E, Nieminen R, Real-time simulation of heat transfer in continuous casting, Metallurgical Transactions B. 1993; 24: 685-93.
[30] Swaminathan C.R, Voller V.R, A general enthalpy method for modeling solidification processes, Metallurgical transactions B. 1992; 23: 651-64.
[31] Mizikar E.A, Mathematical heat transfer model for solidification of continuously cast steel slabs, Transactions of the Metallurgical Society of AIME. 1967; 239: 90-7.
[32] Hong C.P, Computer modelling of heat and fluid flow in materials processing. CRC press; 2019 ; 23.
[33] Ferziger J.H, Perić M, Street R.L, Computational methods for fluid dynamics. springer; 2019.
[34] Nozaki T, Matsuno J.i, Murata K, Ooi H, Kodama M, A secondary cooling pattern for preventing surface cracks of continuous casting slab, Transactions of the Iron and Steel Institute of Japan. 1978; 18(6): 330-8.
[35] Wang X.Y, Liu Q, Wang B, Wang X, Qing J.S, Hu Z.G, Sun Y.H, Optimal control of secondary cooling for medium thickness slab continuous casting. Ironmaking & Steelmaking. 2011; 38(7): 552-60.
[36] Thomas B.G, Behera A.K, Bentsman J, Zheng K, Vapalahti S, Petrus B, Castillejos A.H, Acosta FA. Online dynamic control of cooling in continuous casting of thin steel slabs. InProceedings of NSF Grant conference. 2006.
[37] Ascher U.M, Greif C, editors, A first course on numerical methods, Society for Industrial and Applied Mathematics. 2011.
[38] Hoffman J.D, Frankel S, Numerical methods for engineers and scientists. CRC press; 2018.

ACKNOWLEDGMENTS

This research received no specific grant from funding agencies in the public, commercial, or not-for-profit sectors. The author would like to thank Prof. Rouhollah Tavakoli, a faculty member in the Department of Materials Science and Engineering, at Sharif University of Technology, for his comments, including the offer to utilize the CALPHAD method and the conceptualization of the effect of chemical composition.

CONFLICT OF INTEREST STATEMENT

The author declares that they have no known competing financial interests or personal relationships that could have appeared to influence the work reported in this paper.

Appendix A

Mesh sensitivity analysis is investigated in this section. A numerical simulation based on the data presented in this study was conducted for different mesh densities; see Table A-1. (we considered the steel grade AISI/SAE 1010 here). The temperature values at the slab's central bottom point and infinity norm of the whole thermal field of the slab are calculated at the end of the simulation for each mesh density, as shown in Table A-1. The results of the mesh analysis are shown in Figs. A-1. and Fig. A-2. are based on log-log calculations. According to these graphs and Table A-1. the mesh density 80×200 is optimal (i.e., neither too fine nor too coarse) for numerical simulation in the present study. The graphs show that after the mesh density reaches 8000, or 40×160, the temperature values in the slab's central bottom point and the infinity norm of the whole thermal field of the slab are stable and approach 1345°C and 1551°C, respectively.

Appendix B

The equation $x = K\sqrt{t}$, previously explained in the current work, is extracted from Stephan's problem. It is proven in the literature that the solid shell profile is a square root function of time (or distance from the meniscus), such that there has been a good agreement between numerical results and experiments, see [5, 18, 19]. Therefore, using this square function to estimate the metallurgical length and solid-liquid interface profile is possible. As one of the goals of this work is to find the coefficient K, and we know that K is included in a square root function, we use only two points of the (black) shell profile in schematic Fig. B-1 to make a fitting approximation to find the coefficient K. The points are as follows: the highest solid point on the meniscus located on the lateral side and the last melt droplet (with which the metallurgical length is defined previously) or the first solid point on the central axis of the strand (see the schematic Fig. B-1).

Table A-1. Different mesh density cases, their corresponding temperature in the slab's central bottom point, and their corresponding infinity norm of the whole thermal field of the slab.

Mesh case NO	**#1**	**#2**	**#3**	**#4**	**#5**	**#6**	**#7**	**#8**
n_x	6	8	10	20	30	40	40	40
n_y	16	20	25	50	60	60	80	90
$n_x \times n_y$	96	160	250	1000	1800	2400	3200	3600
T (°C)	1219.51	1248.08	1269.65	1308.51	1322.85	1328.64	1330.38	1333.71
$\|T\|_\infty$(°C)	1539.89	1543.12	1545.54	1549.69	1550.62	1550.62	1550.90	1550.81
Mesh case NO	**#9**	**#10**	**#11**	**#12**	**#13**	**#14**	**#15**	**#16**
n_x	40	40	40	40	40	60	80	160
n_y	100	130	140	150	160	180	200	400
$n_x \times n_y$	4000	5200	5600	6000	8000	10800	16000	64000
T (°C)	1336.51	1339.26	1341.54	1342.58	1343.17	1344.38	1345.07	1345.45
$\|T\|_\infty$(°C)	1550.89	1550.95	1550.97	1550.98	1550.99	1550.99	1550.99	1550.99
Mesh case NO	**#17**	**#18**	**#19**	**#20**	**#21**			
n_x	320	640	1280	2000	2500			
n_y	1200	2400	4800	9600	12000			
$n_x \times n_y$	384000	1536000	6144000	19200000	30000000			
T (°C)	1345.72	1345.83	1345.89	1345.93	1345.94			
$\|T\|_\infty$(°C)	1550.99	1550.99	1550.99	1550.99	1550.99			

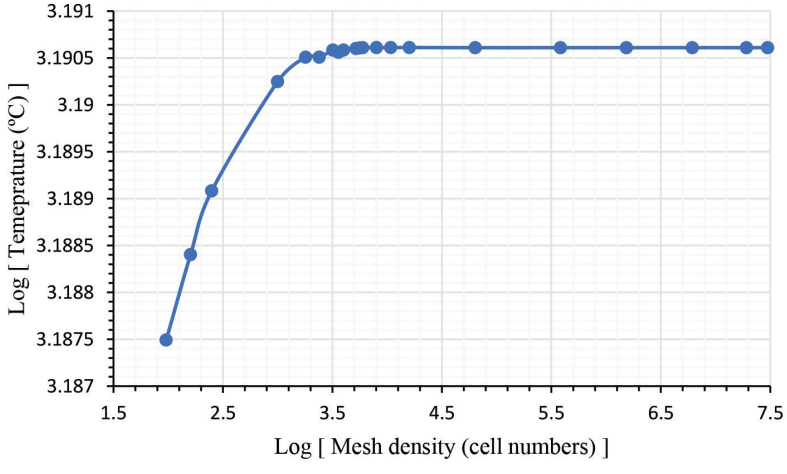

Fig. A-1. Log-log graph of the values of infinity norm of the whole slab thermal field concerning the mesh density at the end of the simulation for AISI/SAE 1010.

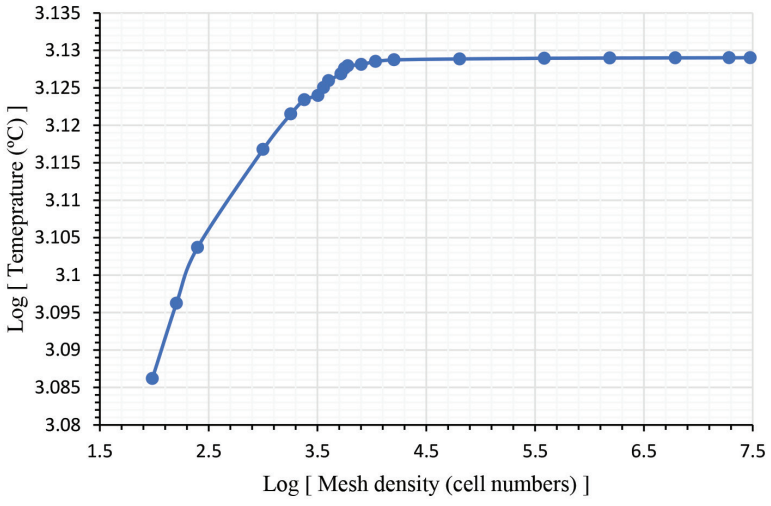

Fig. A-2. Log-log graph of the values of temperature in the slab's central bottom point concerning the mesh density at the end of the simulation for AISI/SAE 1010.

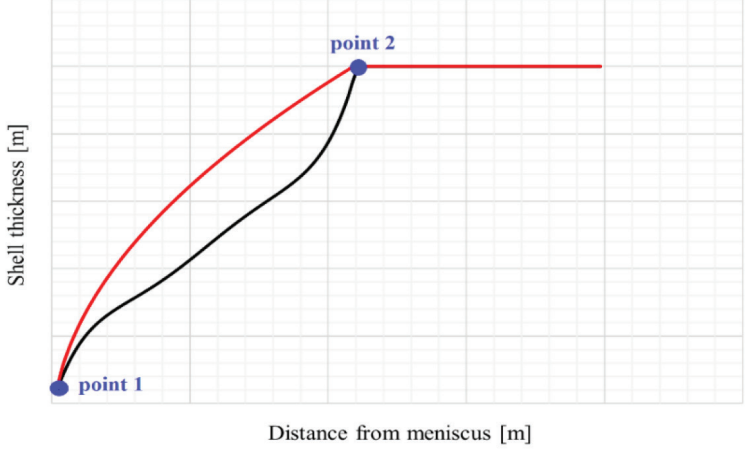

Fig. B-1. Schematic illustration of the fitted curve $x = K\sqrt{t}$ (red) based on points1 and 2 and the corresponding simulation graph (black) obtained from the thermal model of this study.

As $x = K\sqrt{t}$, by considering $t = \frac{D}{v}$ where D denotes the distance from the meniscus, we have the following quadratic equation as

$$D = \left(\frac{v}{K^2}\right)x^2 \qquad \text{Eq.(B-1)}$$

Substituting points 1 and 2 in Eq.(B-1), the following is obtained.

$$\begin{cases} D_1 = \left(\frac{v}{K^2}\right)x_1^2 \\ D_2 = \left(\frac{v}{K^2}\right)x_2^2 \end{cases}$$

Using the above data, we can find the value of K by a simple basic fitting [36, 37] as follows:

$$\begin{bmatrix} D_1 \\ D_2 \end{bmatrix}_{2\times1} = \begin{bmatrix} x_1^2 \\ x_2^2 \end{bmatrix}_{2\times1} \begin{bmatrix} \frac{v}{K^2} \end{bmatrix}_{1\times1} \Rightarrow \begin{bmatrix} D_1 \\ D_2 \end{bmatrix}_{2\times1} = b,$$

$$\begin{bmatrix} x_1^2 \\ x_2^2 \end{bmatrix}_{2\times1} = A, \quad \begin{bmatrix} \frac{v}{K^2} \end{bmatrix}_{1\times1} = X$$

By considering the above system in a matrix form AX=b, we can find the value of K using the least square's theorem in numerical methods [36, 37] as follows:

$$\left[\frac{v}{K^2}\right]_{1\times 1} = X = \left(A^T A\right)^{-1} A^T b \;\Rightarrow\; K = \sqrt{v\left[\left(A^T A\right)^{-1} A^T b\right]^{-1}} \qquad \text{Eq.(B-2)}$$

The standard error and mean relative error of fitting, reported in the current work, are calculated as follows:

$$\text{standard error} = \sqrt{\frac{\sum_{i=1}^{N}\left(x_{\text{fitted}} - x_{\text{simulated}}\right)^2}{N}} \qquad \text{(a)}$$

$$\text{mean relative error} = \frac{1}{N}\sum_{i=1}^{N}\frac{\left|x_{\text{fitted}} - x_{\text{simulated}}\right|}{x_{\text{fit}}} \qquad \text{(b)}$$

Eq.(B-3)